Nr. 85
9. Feb. 2022

universität innsbruck
Institut für Mathematik

Preprint-Series: Department of Mathematics - Applied Mathematics

A Joint Variational Multichannel Multiphase Segmentation Framework

N. Gruber, J. Schwab, S. Court, E. Gizewski, M. Haltmeier

AppliedMathematics

Technikerstraße 13 - 6020 Innsbruck - Austria
Tel.: +43 512 507 53803 Fax: +43 512 507 53898
https://applied-math.uibk.ac.at

manuscript No.
(will be inserted by the editor)

A Joint Variational Multichannel Multiphase Segmentation Framework

Nadja Gruber[1,2] · **Johannes Schwab**[4] · **Sébastien Court**[2] · **Elke Gizewski**[3] · **Markus Haltmeier**[2]

Received: date / Accepted: date

Abstract In this paper, we propose a variational image segmentation framework for multichannel multiphase image segmentation based on the Chan-Vese active contour model. The core of our method lies in finding a variable u encoding the segmentation, by minimizing a multichannel energy functional that combines the information of multiple images. We create a decomposition of the input, either by multichannel filtering, or simply by using plain natural RGB, or medical images, which already consist of several channels. Subsequently we minimize the proposed functional for each of the channels simultaneously. Our model meets the necessary assumptions such that it can be solved efficiently by optimization techniques like the Chambolle–Pock method. We prove that the proposed energy functional has global minimizers, and show its stability and convergence with respect to noisy inputs. Experimental results show that the proposed method performs well in single- and multichannel segmentation tasks, and can be employed to the segmentation of various types of images, such as natural and texture images as well as medical images.

Keywords multichannel segmentation · primal-dual optimization · medical imaging

[1]VASCage-Research Centre on Vascular Ageing and Stroke, Innsbruck, Austria
[2]Department of Applied Mathematics, University of Innsbruck, Austria
[3]Department of Neuroradiology, Medical University of Innsbruck, Austria
[4]MRC Laboratory of Molecular Biology, Hills Road, Cambridge CB2 0QH, UK
E-mail: nadja.gruber@vascage.at

1 Introduction

The fundamental task of image segmentation is the partitioning of an image into regions that are homogeneous according to certain characteristics, such as intensity or texture, by removing all variation except for the edges of image regions. This process plays a fundamental role in many important application fields, such as object detection, recognition and measurement, especially in the area of medical imaging. Many successful methods for image segmentation are based on variational models and active contour models, which share the feature that they find the optimal segmentation as a minimizer of an objective functional, that generally depends on the given image and the traits that are used to identify the different segmented regions. In initial works, the main focus has been on the development of methods for two-phase segmentation, where the goal is to partition a given image into two regions, one representing the object to be detected, and the second one representing the background.

The extension to multiphase image segmentation, i.e. the partitioning of images with multiple regions, constitutes a more challenging problem than two-phase segmentation. In [32] Vese and Chan generalized their two-phase approach proposed in [11] to a multiphase model, by using multiple level-set functions operating on the same image. Both, piecewise constant and piecewise smooth cases, are studied. The advantage of using level-set functions to represent the regions is that the problems of vacuum and overlap are automatically eliminated. However, this method has several drawbacks such as slow convergence, the fact that multiple regions can not be handled in a straightforward manner, and the possible convergence towards undesirable local minima.

The method we propose is inspired from the Chan-Vese approach, and addresses the challenge of achieving efficiently the multichannel multiphase segmentation task. For the latter, we prove rigorously existence of solutions, stability and convergence. We also provide efficient implementation and experimental simulations that demonstrate the applicability of our method.

The paper is structured as follows. In Section 2, we will briefly review some of the most fundamental two-phase segmentation functionals, their extensions to multiphase models and some more recent works which are related to the proposed method. We then introduce the proposed method in Section 3 and present the associated mathematical analysis in the subsequent section. In Section 5 we discuss details of the numerical implementation and optimization of our method. Then, in Section 6, we demonstrate the possible applications and experimental results, before finally discussing drawn conclusions and future plans in Section 7.

2 Background

In this section, we briefly review some of the most fundamental two-phase segmentation functionals from the literature, their extensions to multiphase models and some more recent works that are related to the method proposed in the present article. More specifically, we consider region-based segmentation methods that identify regions, based on similarities of their pixels.

2.1 The Mumford-Shah Model and its level-set Representation

Let us give a brief overview of the multiphase and multichannel image segmentation methods existing in the literature. One of the most popular region-based segmentation models is the Mumford-Shah model proposed in 1989 [26]. In the following, Ω denotes a bounded, open set with Lipschitz boundary, and $f : \Omega \to [0, 1]$ the given image. The idea of Mumford and Shah consists in solving segmentation and denoising problems by minimizing an energy functional with respect to a closed contour $\Gamma \subset \Omega$, that partitions Ω into subregions Ω_i, $i = 1, \dots, K$ (in the two-phase case $K = 2$) and a function $u \in H^1(\Omega \setminus \Gamma)$. The proposed energy functional is of the form

$$E_{\mathrm{MS}}(u, \Gamma; \Omega) = \nu|\Gamma| + \lambda \int_{\Omega\setminus\Gamma} |\nabla u|^2 \,\mathrm{d}x + \int_{\Omega} (u - f)^2 \,\mathrm{d}x, \quad \nu, \lambda, > 0. \tag{1}$$

In E_{MS} the first term penalizes the length $|\Gamma|$ of Γ, the second term enforces the smoothness of u in $\Omega \setminus \Gamma$, and the last term is the fidelity term controlling the distance of u to the given image f. Finding a minimizer of the non-convex and non-smooth Mumford-Shah functional (1) constitutes a challenging task, and many approaches to simplify model (1) have been meanwhile proposed. In [1, 2, 4] it is described how the simplification has been achieved by approximating (1) by a sequence of simpler elliptic variational problems, where the length term Γ was replaced by a phase field energy. A detailed mathematical study of the Mumford-Shah approach is given in [23]. In the simplest form of the model, u is assumed to be constant on each segment, meaning that the second term in the functional (1) vanishes. The model then reduces to the so-called piecewise constant Mumford-Shah Model (PCMS)

$$E_{\mathrm{PCMS}}(u, \Gamma; \Omega) = \nu|\Gamma| + \lambda \int_{\Omega} (u - f)^2 \,\mathrm{d}x. \tag{2}$$

Assuming that $\Omega = \bigcup_{i=1}^{K} \Omega_i$ with pairwise disjoint sets Ω_i and piecewise constant functions $u_i(x) = c_i$ on Ω_i, $i = 1, \dots, K$, model (2) can be rewritten as

$$E_{\mathrm{PCMS}}(\boldsymbol{\Omega}, \boldsymbol{c}) = \frac{1}{2} \sum_{i=1}^{K} \mathrm{Per}(\Omega_i, \Omega) + \lambda \sum_{i=1}^{K} \int_{\Omega_i} (c_i - f)^2 \,\mathrm{d}x,$$

where $\boldsymbol{\Omega} \coloneqq \{\Omega_i\}_{i=1}^{K}, \boldsymbol{c} \coloneqq \{c_i\}_{i=1}^{K}$, and $\mathrm{Per}(\Omega_i, \Omega)$ denotes the perimeter of Ω_i in Ω, i.e. $\mathrm{Per}(\Omega_i, \Omega) = |\partial\Omega_i \cap \Omega|$. If the number of phases is 2, i.e. $K = 2$, the PCMS model reduces to the Chan-Vese model [11]

$$E_{\mathrm{CV}}(\Gamma, c_0, c_1) = \nu|\Gamma| + \lambda\left[\int_{\Omega_1} (c_0 - f)^2 \,\mathrm{d}x + \int_{\Omega_2} (c_1 - f)^2 \,\mathrm{d}x\right], \tag{3}$$

where c_0 and c_1 are two constants, denoting the mean value of the image inside and outside the curve Γ, respectively.

In [11], the authors reformulate and solve (3) using the level-set method [27]. In the level-set method, $\Gamma \subset \Omega$ is represented by the zero level-set of a Lipschitz function. More precisely, Γ, Ω_1 and Ω_2 are given in terms of the Lipschitz function $\phi : \Omega \to \mathbb{R}$ as follows

$$\begin{aligned} \Gamma &= \{x \in \Omega : \phi(x) = 0\}, \\ \Omega_1 &= \{x \in \Omega : \phi(x) > 0\}, \\ \Omega_2 &= \{x \in \Omega : \phi(x) < 0\}. \end{aligned}$$

Then, each term in energy (3) can be expressed in terms of ϕ and the Heaviside function H as below

$$E_{\mathrm{CV}}(\phi, c_0, c_1) = \nu \int_\Omega |\nabla H(\phi)| \, \mathrm{d}x + \lambda \int_\Omega H(\phi)\big(c_0 - f\big)^2 \, \mathrm{d}x + \lambda \int_\Omega \big(1 - H(\phi)\big)\big(c_1 - f\big)^2 \, \mathrm{d}x, \tag{4}$$

where the gradient operator ∇ is taken in the sense of distributions. The variational formulation in the Chan-Vese model is non-convex, which implies that a standard gradient-descent implementation is not guaranteed to converge to a global minimum.

To overcome this drawback, a convex relaxation approach was proposed in [9]. More precisely, it was shown in [9] that for fixed $c_0, c_1 \in \mathbb{R}$ a global minimizer of (4) can be found by considering the following convex minimization problem:

$$\min_{0\le u\le 1} \nu \int_\Omega |\nabla u| \, \mathrm{d}x + \lambda \int_\Omega \Big[(c_0 - f)^2 - (c_1 - f)^2\Big] u \, \mathrm{d}x. \tag{5}$$

Subsequently we have $\Omega_1 = \{x : u(x) \ge \mu\}$ for a.e. $\mu \in [0, 1]$. Since Problem (5) is convex, it allows efficient computation of global minimizers for the Chan-Vese model (4).

2.2 Contributions related to our approach

While in the previous paragraphs we discussed the partitioning of a single image into two regions, we now present some of the multichannel and multiphase extensions that have been proposed. The Chan-Vese model described in Section 2.1 was initially expanded to vector valued systems [10]. This allowed combining multiple images simultaneously to segment the images and identify the key object. The resulting algorithm is of particular interest for managing the segmentation of RGB images, where intensity detectors and channel-by-channel boundary detectors fail.

2.2.1 Multichannel Extension in Chan-Vese Model

Let f_i be the i-th channel of an image on Ω, with $i = 1, \ldots, K$ channels, and the level-set function ϕ as in (4). Each channel would contain the same image with some differences, for instance different frequencies at which the image was taken, color images, etc. Denote by $\bar{c}_0 = (c_{0,1}, \ldots, c_{0,K})$ and $\bar{c}_1 = (c_{1,1}, \ldots, c_{1,K})$ two unknown, constant vectors.

The extension of the Chan-Vese model (4) to the vector-valued case [10] is given by

$$E_{\mathrm{CV}}(\phi, \bar{c_0}, \bar{c_1}) = \nu \int_\Omega |\nabla H(\phi)| + \frac{1}{K} \sum_{i=1}^{K} \Big[\int_\Omega H(\phi)\big(c_{0,i} - f_i\big)^2 \, \mathrm{d}x + \int_\Omega \big(1 - H(\phi)\big)\big(c_{1,i} - f_i\big)^2 \, \mathrm{d}x \Big].$$

As in the scalar case, the model searches for the best vector-valued approximation taking only two values. The active contour is the boundary between these two regions.

2.2.2 Multiphase Active Contours without edges

The initial multiphase algorithm follows the natural extension of the piecewise constant Mumford-Shah functional for n phases

$$E^n_{\mathrm{PCMS}}(u, \Gamma, \Omega) = \sum_{i=1}^{n} \int_{\Omega_i} (c_i - f)^2 + \nu |\Gamma|,$$

where Ω_i's are the connected components of $\Omega \setminus \Gamma$, $u = c_i$ on Ω_i and $\Gamma = \bigcup_{i=1}^n \partial\Omega_i$. In [32] Vese and Chan proposed to rewrite this in level-set form. The classes are labelled by i, with $1 \le i \le 2^m = n$. The constant vector of averages is denoted by $c = (c_1, \ldots, c_n)$, where c_i, $i = 1, \ldots, n$ is the mean value of f in class i and χ_i denotes the characteristic function for each class i. The energy which is minimized is given by:

$$E_n(\boldsymbol{\phi}, \boldsymbol{c}) = \sum_{1\le i\le n=2^m} \int_\Omega (c_i - f)^2 \chi_i \, \mathrm{d}x + \sum_{1\le j\le m} \nu \int_\Omega |\nabla H(\phi_j)|.$$

Here, the set of curves Γ is represented by the union of the zero level-sets of the functions ϕ_j. Clearly, for the case $n = 2$ (and therefore $m = 1$) we obtain the 2-phase energy (4) considered in the active contour model without edges.

2.2.3 Multichannel Multiphase Extension

In [32] the authors extended the proposed multiphase model to vector-valued images.

In the resulting multichannel multiphase approach, the initial data $f = (f_1, \ldots, f_K)$ consists of K channels and for each channel one has constants $\boldsymbol{c}_j = (c_{1,j}, \ldots c_{n,j})$,

where $c_{i,j}$ is the mean value of f_j in class i. In this case, the model has the following form

$$E_n(\boldsymbol{\phi}, \boldsymbol{c}_i) = \sum_{1\le i\le n=2^m} \sum_{j=1}^{K} \int_\Omega (c_{i,j} - f_j)^2 \chi_i \,\mathrm{d}x + \sum_{1\le j\le m} \nu \int_\Omega |\nabla H(\phi_j)|.$$

The level-set functions are the same for all channels, i.e. no additional level-set function for each channel is needed. However, all of this proposed multichannel and multiphase models suffer from the existence of undesirable local minima, and the strong sensitivity of the results with respect to initialization.

A more recent extension of the aforementioned two-phase approaches is proposed in [21], where the authors develop a multiphase image segmentation method based on fuzzy region competition [25, 35]. They start from the general N-phase region competition functional, introduce fuzzy membership functions and replace the error term by the data fidelity of the Mumford-Shah and Chan-Vese model, respectively. In [24] the relaxed version of the Chan-Vese two-phase piecewise constant energy minimization formulation is extended to the four-phase domain with application to medical image segmentation. Though in both works, the existence of minimizers of the resulting energy functionals is proved, in the present paper we investigate stability and convergence with respect to noisy inputs.

Another interesting method is proposed by Cai et. al in [6]. Inspired by the observation that binary images can be recovered quite well from their smoothed versions by thresholding, they propose a two-stage segmentation method based on the Mumford-Shah model, where the first stage consists in finding a smooth solution to a convex variant of the Mumford-Shah model, and in the second stage a thresholding strategy is applied in order to reveal different segmentation features.

In the literature many more multiphase segmentation algorithms that are related to the Chan-Vese or Mumford-Shah model can be found, see e.g. [5, 30, 34]. Nevertheless, nearly all of these methods restrict to the information coming from one single image while in our work we are considering an algorithm that exploits the increased information of multiple image inputs which goes beyond the three RGB channels. Furthermore we present a novel mathematical analysis of stability with respect to the distorted input images and examine convergence behaviour if the distortion tends to zero.

2.3 Our contributions

In this paper, we introduce a segmentation functional for multichannel multiphase image segmentation for which we provide mathematical analysis. The proposed framework can be used for multichannel image segmentation, where the channels may be obtained from a single image or from multiple images. More precisely, we make the following contributions:

- We use feature maps obtained by pre-filtering and minimize our proposed energy functional to divide the image into regions. Our model can distinguish between up to $K+1$ different regions, where K denotes the number of channels.
- The proposed energy functional allows segmentation of one single image or multiple images, and prevents the regions found from overlapping. This implies that in case where the division of images into several specific regions is generally mastered by combining different images, as it occurs in medical imaging, this method is particularly useful. Compared with the Chan-Vese functional, the one we consider is smoother, facilitating the algorithmic solving and its implementation. It also offers more flexibility, as the corresponding multiphase segmentation is then based on the number of channels, rather than on the number of level-sets to consider.
- We propose an efficient implementation of the method and apply the first-order primal-dual algorithm proposed by Chambolle and Pock in [8] to the constrained total variation (TV) minimization problem.
- One of the main emphases of this paper lies on the theoretical analysis of the proposed energy functional: We prove the existence of minimizers, and show stability and convergence. As far as we know, no stability nor convergence result exist when considering the Chan-Vese functional.
- A major advantage of the proposed method is that it can be efficiently combined with a deep learning approach (see e.g. [16, 18, 19, 28] for an overview of some combined methods). The capacity of neural networks of extracting meaningful feature representations of images can be combined with the mathematical elegance and efficiency of a fully analysed variational model. Thus we can exploit the advantages of both worlds.

The aim of this paper is to provide a flexible framework for each kind of multichannel-multiphase image segmentation, which is particularly relevant for medical image segmentation problems.

3 The Proposed Method

Let $\Omega \subset \mathbb{R}^2$ be a bounded domain with Lipschitz boundary, and $f = (f_i)_{i=1}^K : \bar{\Omega} \to [0,1]^K$ denote the given images. In what follows $BV(\Omega)$ denotes the space of functions of bounded variation on Ω, i.e. the Banach space of functions $u : \Omega \to [0,1]$ with finite norm $\|u\|_{BV} := \|u\|_{L^1(\Omega)} + TV(u)$, where

$$TV(u) := \sup\Big\{ \int_\Omega u(x) \operatorname{div} \phi \, \mathrm{d}x \mid \phi \in \mathcal{C}_c^1(\Omega, \mathbb{R}^2), \|\phi\|_\infty \le 1 \Big\}.$$

The derivative Du of u in the sense of distributions is a vector-valued Radon measure having total mass $|Du|(\Omega) := \int_\Omega |Du| \, \mathrm{d}x = TV(u)$, see [12, 13] for more details. The main advantage of applying total variation regularization is its ability to preserve sharp edges in the image.

The proposed constrained energy minimization problem is of the following form

$$\min_{u,\mathbf{c}} \Bigg(E(u, \mathbf{c}, f) := \sum_{i=1}^K \int_\Omega (c_{1,i} - f_i)^2 u_i \, \mathrm{d}x + \sum_{i=1}^K \int_\Omega (c_{2,i} - f_i)^2 (1 - u_i) \, \mathrm{d}x + \lambda \int_\Omega |Du_i| \mathrm{d}x \Bigg)$$

subject to

$$\sum_{i=1}^K u_i \le 1, \;\; 0 \le u_i, \quad \forall i = 1, \dots, K, \tag{6}$$

and is jointly minimized over $(u_i)_{i=1}^K \in BV(\Omega, [0,1]^K)$ and $\mathbf{c} = (c_i)_{i=1}^K \in \mathbb{R}^{2K}$, where $c_i = (c_{1,i}, c_{2,i}) \in \mathbb{R}^2$. The regularization parameter is given by $\lambda \ge 0$ and K denotes the number of channels. Further, f_i for $i = 1, \dots, K$ denote either feature maps extracted from the input image f via filtering, or several channels, which are provided by the imaging modality. Further, it is worth mentioning, that Problem 6 is bi-convex.

If $\int_\Omega u_i(x) \, \mathrm{d}x > 0$, from the Karush-Kuhn-Tucker conditions, one can derive that for any fixed $u \in BV(\Omega, [0,1]^K)$, the following two expressions minimize (6):

$$c_{1,i}(u_i) = \frac{\int_\Omega f_i u_i \, \mathrm{d}x}{\int_\Omega u_i \, \mathrm{d}x}, \quad c_{2,i}(u_i) = \frac{\int_\Omega f_i (1 - u_i) \, \mathrm{d}x}{\int_\Omega (1 - u_i) \, \mathrm{d}x}, \tag{7}$$

Otherwise, if $\int_\Omega u_i(x) = 0$, i.e. ($u_i(x) = 0$ a.e. $x \in \Omega$) and $\int_\Omega u_j(x) > 0$ for some $j \ne i$, we set $c_{1,i}(u_i) = 0$. The same holds for $1 - u_i$ and the corresponding mean value $c_{2,i}(u_i)$. If $f_i = 0$, and hence $c_{1,i}(u_i) = c_{2,i}(u_i) = 0$ for $i = 1, \dots, K$, then $u_1 = 1$ and $u_j = 0, j = 2, \dots, K$ is a minimizer of Problem (6).

In what follows, we denote $\boldsymbol{c}(u) = (c_1(u), c_2(u)) \in \mathbb{R}^K \times \mathbb{R}^K$. Then, for the sake of simplicity, instead of Problem (6), we rather consider

$$\min_u \big(\underline{\mathrm{E}}(u, f) := E(u, \boldsymbol{c}(u), f) \big) \quad \text{subject to} \quad \sum_{i=1}^K u_i \le 1, \;\; 0 \le u_i, \quad \forall i = 1, \dots, K. \tag{8}$$

Explicitly, we have

$$\underline{\mathrm{E}}(u, f) = \sum_{i=1}^K \int_\Omega (c_{1,i}(u_i) - f_i)^2 u_i \, \mathrm{d}x + \sum_{i=1}^K \int_\Omega (c_{2,i}(u_i) - f_i)^2 (1 - u_i) \, \mathrm{d}x + \lambda \int_\Omega |Du_i| \, \mathrm{d}x.$$

Equivalence of Problems (6) and (8) is established in the following result.

Theorem 1 *Let $f = (f_i)_{i=1}^K \in L^\infty(\Omega, [0,1])^K$ and assume there exist minimizers in $BV(\Omega, [0,1]^K)$ satisfying the constraints in* (6)*. Then* (6) *and* (8) *are equivalent, i.e.*

$$\hat{u} \in \arg\min_u \underline{E}(u, f) \Leftrightarrow (\hat{u}, \boldsymbol{c}(\hat{u})) \in \arg\min_{u,\boldsymbol{c}} E(u, \boldsymbol{c}, f).$$

Proof Let $\hat{u} \in \arg\min_u \underline{\mathrm{E}}(u, f)$ and let us assume that $(\hat{u}, \boldsymbol{c}(\hat{u})) \notin \arg\min_{u,\boldsymbol{c}} E(u, \boldsymbol{c}, f)$. Then there exists $(\tilde{u}, \tilde{\boldsymbol{c}}) \ne (\hat{u}, \boldsymbol{c}(\hat{u}))$ satisfying

$$E(\tilde{u}, \tilde{\boldsymbol{c}}, f) < E(\hat{u}, \boldsymbol{c}(\hat{u}), f). \tag{9}$$

For $\tilde{u} \ne \hat{u}$ it holds by optimality of $\boldsymbol{c}(\cdot)$ given by (7) that

$$E(\tilde{u}, \boldsymbol{c}(\tilde{u}), f) \le E(\tilde{u}, \tilde{\boldsymbol{c}}, f) < E(\hat{u}, \boldsymbol{c}(\hat{u}), f) \tag{10}$$

Since $E(\tilde{u}, \boldsymbol{c}(\tilde{u}), f) = \underline{\mathrm{E}}(\tilde{u}, f)$ and $E(\hat{u}, \boldsymbol{c}(\hat{u}), f) = \underline{\mathrm{E}}(\hat{u}, f)$, inequality (10) would imply that $\underline{\mathrm{E}}(\tilde{u}, f) < \underline{\mathrm{E}}(\hat{u}, f)$ which contradicts $\hat{u} \in \arg\min_u \underline{\mathrm{E}}(u, f)$.

For $\tilde{u} = \hat{u}$ and $\tilde{\boldsymbol{c}} \ne \boldsymbol{c}(\hat{u})$ again it holds by the definition of $\boldsymbol{c}(\cdot)$ that

$$E(\tilde{u}, \tilde{\boldsymbol{c}}, f) = E(\hat{u}, \tilde{\boldsymbol{c}}, f) \ge E(\hat{u}, \boldsymbol{c}(\hat{u}), f),$$

which contradicts (9). Conversely, let $(\hat{u}, \hat{\boldsymbol{c}}) \in \arg\min_{u,\boldsymbol{c}} E(u, \boldsymbol{c}, f)$ and let us assume that $\hat{u} \notin \arg\min_u \underline{\mathrm{E}}(u, f)$. Then there exists $\tilde{u}$ with $\tilde{u} \ne \hat{u}$ such that

$$\underline{\mathrm{E}}(\tilde{u}, f) < \underline{\mathrm{E}}(\hat{u}, f).$$

Consequently,

$$\underline{\mathrm{E}}(\tilde{u}, f) = E(\tilde{u}, \boldsymbol{c}(\tilde{u}), f) < \underline{\mathrm{E}}(\hat{u}, f) = E(\hat{u}, \boldsymbol{c}(\hat{u}), f) \le E(\hat{u}, \hat{\boldsymbol{c}}, f),$$

which contradicts $(\hat{u}, \hat{\boldsymbol{c}}) \in \arg\min_{u,\boldsymbol{c}} E(u, \boldsymbol{c}, f)$. □

For the sake of concision, we will denote

$$\underline{\mathrm{E}}(u,f) = \mathcal{F}(u,f) + \lambda\mathcal{R}(u),$$

where

$$\begin{aligned}\mathcal{F}(u,f) &\coloneqq \sum_{i=1}^{K}\int_\Omega \big(c_{1,i}(u_i)-f_i\big)^2 u_i\,\mathrm{d}x \\ &\qquad + \int_\Omega \big(c_{2,i}(u_i)-f_i\big)^2(1-u_i)\,\mathrm{d}x,\\ \mathcal{R}(u) &\coloneqq \sum_{i=1}^{K}\int_\Omega |Du_i|\,\mathrm{d}x.\end{aligned}$$

This sets all the basic notation and in the following section we study existence of minimizers, stability with respect to distorted input and convergence behaviour if the distortion tends to zero.

4 Mathematical Analysis

Under the assumption that $f \in L^\infty(\Omega,[0,1]^K)$, the energy (6) is well defined for the admissible set

$$\mathcal{D}(\underline{\mathrm{E}}) \coloneqq \left\{ u \in BV(\Omega,[0,1]^K) \mid 0 \le u_i\,, \sum_{i=1}^{K} u_i \le 1 \right\}.$$

Before we start the analysis, we recall Rellich's compactness theorem for BV functions.

Theorem 2 *Let $\Omega \subset \mathbb{R}^n$ be a bounded domain with Lipschitz-boundary, and let $\{u_n\}_{n\in\mathbb{N}}$ be a sequence of functions in $BV(\Omega)$ such that $sup_n\|u_n\|_{BV} < \infty$. Then there exists $u \in BV(\Omega)$ and a subsequence $\{u_{n_k}\}_{k\in\mathbb{N}}$ such that $u_{n_k} \to u$ (strongly) in $L^1(\Omega)$ as $k \to \infty$.*

Proof See [3, Theorem 3.23, page 132].

In the following, we prove the existence and stability of minimizers of (6), and examine their convergence behavior.

Theorem 3 (Existence) *Let $f \in L^\infty(\Omega,[0,1]^K)$ be a given image with K channels. Then, for $\lambda \ge 0$, energy $\underline{E}$ admits at least one global minimizer in $\mathcal{D}(\underline{E})$.*

Proof It is clear that for all $u \in \mathcal{D}(\underline{\mathrm{E}})$ it holds that $\underline{\mathrm{E}}(u,f) \ge 0$. Further if $u_i(x) = \frac{1}{K}$ for all $x \in \Omega$, we have $c_{1,i} = c_{2,i} = \frac{1}{|\Omega|}\int_\Omega f_i\,\mathrm{d}x$, and thus

$$\begin{aligned}\underline{\mathrm{E}}(u,f) &= \sum_{i=1}^{K}\int_\Omega \big(c_{1,i}(u_i)-f_i\big)^2\,\mathrm{d}x \\ &\qquad + \int_\Omega \big(c_{2,i}(u_i)-f_i\big)^2\,\mathrm{d}x\\ &= 2\sum_{i=1}^{K}\int_\Omega \Big(\frac{1}{|\Omega|}\int_\Omega f_i\,\mathrm{d}x - f_i\Big)^2\,\mathrm{d}x \\ &\le 2\sum_{i=1}^{K}\int_\Omega \Big(\frac{|\Omega|\|f_i\|_\infty}{|\Omega|} + \|f_i\|_\infty\Big)^2\,\mathrm{d}x\\ &= 8|\Omega|\sum_{i=1}^{K}\|f_i\|_\infty^2 < L(f) < \infty,\end{aligned} \tag{11}$$

where $L(f)$ denotes a positive constant which only depends on the image f. Therefore we have for $a \coloneqq \inf_u \underline{\mathrm{E}}(u,f)$ that $0 \le a < \infty$. Now let $\{u^n\}_{n\in\mathbb{N}} \subset \mathcal{D}(\underline{\mathrm{E}})$ be a sequence such that $\underline{\mathrm{E}}(u^n,f) \to a$. Then there exists a constant $M > 0$ such that

$$\begin{aligned}\underline{\mathrm{E}}(u^n,f) = \sum_{i=1}^{K}\Big(&\int_\Omega (c_{1,i}(u_i^n)-f_i)^2 u_i^n\,\mathrm{d}x\\ &+ \int_\Omega (c_{2,i}(u_i^n)-f_i)^2(1-u_i^n)\,\mathrm{d}x\Big)\\ &+ \lambda\int_\Omega |Du_i^n|\,\mathrm{d}x \le M\end{aligned}$$

and therefore in particular

$$\lambda\int_\Omega |Du_i^n|\,\mathrm{d}x \le M. \tag{12}$$

Since u_i^n have values in $[0,1]$ for all $i = 1,\dots,K$, we have that $\int_\Omega u_i^n\,\mathrm{d}x \le |\Omega|$, which together with (12) implies that $\{u_i^n\}_{n\in\mathbb{N}}$ is uniformly bounded in $\mathcal{D}(\underline{\mathrm{E}})$. By Theorem 2 there exists a subsequence u_i^n that (strongly) converges to a function $\hat{u}_i \in BV(\Omega,[0,1])$ such that

$$u_i^n \to \hat{u}_i \quad \text{strongly in } L^1(\Omega).$$

Up to a subsequence, we may assume that u_i^n converges to $\hat{u}_i$ pointwise a.e., i.e.

$$u_i^n(x) \to \hat{u}_i(x) \quad \text{a.e..}$$

Since for $i = 1,\dots,K$ the u_i^n satisfy the constraints, $\hat{u}_i$ satisfies these properties too, and thus we conclude that $\hat{u} \in \mathcal{D}(\underline{\mathrm{E}})$. Further we obtain the following inequalities

$$0 \le c_{1,i}(u_i^n) = \frac{\int_\Omega f_i u_i^n\,\mathrm{d}x}{\int_\Omega u_i^n\,\mathrm{d}x} \le \int_\Omega f_i\,\mathrm{d}x,$$

and (13)

$$0 \le c_{2,i}(u_i^n) = \frac{\int_\Omega f_i(1-u_i^n)\,\mathrm{d}x}{\int_\Omega (1-u_i^n)\,\mathrm{d}x} \le \int_\Omega f_i\,\mathrm{d}x.$$

This implies that the sequences $\{c_{1,i}(u_i^n)\}_{n\in\mathbb{N}}$ and $\{c_{2,i}(u_i^n)\}_{n\in\mathbb{N}}$ are uniformly bounded, and hence there exist subsequences also denoted by $\{c_{1,i}(u_i^n)\}_{n\in\mathbb{N}}$ and $\{c_{2,i}(u_i^n)\}_{n\in\mathbb{N}}$ such that

$$c_{1,i}(u_i^n) \to \hat{c}_{1,i} \quad \text{and} \quad c_{2,i}(u_i^n) \to \hat{c}_{2,i}$$

uniformly. Since $u_i^n \to \hat{u}_i$ a.e. in Ω, Fatou's Lemma yields

$$\begin{aligned}\int_\Omega (\hat{c}_{1,i} - f_i)^2 \hat{u}_i \,\mathrm{d}x + \int_\Omega (\hat{c}_{2,i} - f_i)^2 (1-\hat{u}_i)\,\mathrm{d}x \\ \leq \liminf_{n\to\infty} \int_\Omega (c_{1,i}(u_i^n) - f_i)^2 u_i^n \,\mathrm{d}x \\ + \int_\Omega (c_{2,i}(u_i^n) - f_i)^2 (1-u_i^n)\,\mathrm{d}x. \quad (14)\end{aligned}$$

By the lower semi-continuity of total variation [14, Theorem 1.9, page 7] it holds that

$$\int_\Omega |D\hat{u}_i| \,\mathrm{d}x \leq \liminf_{n\to\infty} \int_\Omega |Du_i^n| \,\mathrm{d}x. \quad (15)$$

Combining (14) and (15) for all i, on a suitable subsequence, we have established that

$$\underline{\mathrm{E}}(\hat{u}, f) \leq \liminf_{n\to\infty} \underline{\mathrm{E}}(u^n, f) = \inf_n \underline{\mathrm{E}}(u^n, f) = a.$$

Hence $\hat{u} \in \mathcal{D}(\underline{\mathrm{E}})$ is a minimizer of $\underline{\mathrm{E}}$. □

Next we investigate the stability behavior of the solutions so found. This ensures that, for a given regularization parameter λ, the regularized solution $\hat{u}$ depends continuously on f.

Theorem 4 (Stability) *Let $f \in L^\infty(\Omega, [0,1]^K)$ denotes the given image with K channels and $\{f^n\}_{n\in\mathbb{N}}$ a sequence such that $\|f^n - f\|_\infty \to 0$. Further let $\{u^n\}_{n\in\mathbb{N}}$ be a sequence of minimizers of $\underline{E}(u, f^n)$. Then $\{u^n\}_{n\in\mathbb{N}}$ has a convergent subsequence and each limit of a converging subsequence is a minimizer of $\underline{E}(u, f)$.*

Proof Let $u^n \in \arg\min_{u\in\mathcal{D}(\underline{\mathrm{E}})} \underline{\mathrm{E}}(u, f^n)$. We have

$$\underline{\mathrm{E}}(u^n, f^n) \leq \underline{\mathrm{E}}(u, f^n).$$

Let $u_i(x) = \frac{1}{K}$ for all $x \in \Omega$. Then we obtain for all $n \in \mathbb{N}$:

$$\begin{aligned}\underline{\mathrm{E}}(u^n, f^n) &\leq 2\sum_{i=1}^K \int_\Omega \left(f_i^n - \frac{\int_\Omega f_i^n \,\mathrm{d}x}{|\Omega|} \right)^2 \mathrm{d}x \\ &\leq 2\sum_{i=1}^K \int_\Omega \left(f_i^n - f_i + f_i - \frac{\int_\Omega f_i^n - f_i + f_i \,\mathrm{d}x}{|\Omega|} \right)^2 \mathrm{d}x \\ &\leq 2\sum_{i=1}^K \int_\Omega \left(|f_i^n - f_i| + |f_i| + \frac{\int_\Omega |f_i^n - f_i| + |f_i| \mathrm{d}x}{|\Omega|} \right)^2 \mathrm{d}x.\end{aligned}$$

Since $\|f^n - f\|_\infty \to 0$ for n large enough, we have

$$\underline{\mathrm{E}}(u^n, f^n) \leq 2\sum_{i=1}^K \int_\Omega \left(1 + |f_i| + \frac{\int_\Omega |f_i| \,\mathrm{d}x}{|\Omega|} \right)^2 \mathrm{d}x < \infty.$$

Thus, u^n is bounded in $BV(\Omega, [0,1]^K)$. This implies, that there exists a subsequence also denoted by $\{u^n\}_{n\in\mathbb{N}}$ such that

$$u^n \to \hat{u} \in BV(\Omega, [0,1]^K).$$

Similar to (13) we have for all $n \in \mathbb{N}$ and $k \in \{1, 2\}$

$$|c_{k,i}(u_i^n)| \leq \int_\Omega |f_i^n| dx \leq \int_\Omega |f_i^n - f_i| + |f_i|.$$

For n large enough we then have

$$|c_{k,i}(u_i^n)| \leq \int_\Omega \left(\frac{1}{2} + |f_i| \right) \mathrm{d}x < \infty.$$

This shows that the $c_{k,i}(u_i^n)$ sequences are bounded and have convergent subsequences

$$c_{1,i}(u_i^n) \to \hat{c}_{1,i} \in \mathbb{R}, \quad c_{2,i}(u_i^n) \to \hat{c}_{2,i} \in \mathbb{R}.$$

It remains us to show that $\hat{u}$ is a minimizer of $\underline{\mathrm{E}}(u, f)$. By lower semi-continuity of TV we have

$$\lambda\mathcal{R}(\hat{u}) \leq \liminf_{n\to\infty} \lambda\mathcal{R}(u^n). \quad (16)$$

Since $u_i^n \to \hat{u}_i$, a.e., $c_{i,k}(u_i^n) \to \hat{c}_{i,k}$ and $f_i^n \to f$, by using the optimal representations for $c_{1,i}$ and $c_{2,i}$ and Fatou's lemma we obtain

$$\begin{aligned}\mathcal{F}(\hat{u}, f) \leq &\sum_{i=1}^K \int_\Omega \left(\hat{c}_{1i} - f_i\right)^2 \hat{u}_i \,\mathrm{d}x \\ &+ \int_\Omega \left(\hat{c}_{2,i} - f_i\right)^2 (1-\hat{u}_i)\,\mathrm{d}x \\ &\leq \liminf_{n\to\infty} \Big(\sum_{i=1}^K \int_\Omega \left(c_{1,i}(u_i^n) - f_i^n\right)^2 u_i^n \,\mathrm{d}x \\ &+ \int_\Omega \left(c_{2,i}(u_i^n) - f_i^n\right)^2 (1-u_i^n)\,\mathrm{d}x \Big).\end{aligned}$$

Using this last inequality and (16), we conclude that for $\hat{u} \in \mathcal{D}(\underline{\mathrm{E}})$ the following holds for all u

$$\begin{aligned}\underline{\mathrm{E}}(\hat{u}, f) &= \mathcal{F}(\hat{u}, f) + \lambda\mathcal{R}(\hat{u}) \\ &\leq \liminf_{n\to\infty} \mathcal{F}(u^n, f^n) + \lambda\mathcal{R}(u^n) \\ &\leq \limsup_{n\to\infty} \mathcal{F}(u^n, f^n) + \lambda\mathcal{R}(u^n) \\ &\leq \lim_{n\to\infty} \mathcal{F}(u, f^n) + \lambda\mathcal{R}(u) \\ &= \mathcal{F}(u, f) + \lambda\mathcal{R}(u) \\ &= \underline{\mathrm{E}}(u, f),\end{aligned}$$

and thus, $\hat{u} \in \mathcal{D}(\underline{\mathrm{E}})$ is a minimizer of the energy $\underline{\mathrm{E}}(u, f)$. □

In the following, we will examine the fidelity term in more detail to determine which requirements the image f must meet so that $\mathcal{F}$ has an exact solution, i.e. that there is some $u \in \mathcal{D}(\underline{\mathrm{E}})$ such that $\mathcal{F}(u, f) = 0$. This is of particular interest for the convergence analysis.

Theorem 5 *Let $f \in L^\infty(\Omega)$ be an image with only one channel. Then the fidelity term $\mathcal{F}(u, f)$ vanishes if and only if f is either constant or takes only two values. If f is not constant, solutions u^* satisfying $\mathcal{F}(u^*, f) = 0$ are binary. If f is constant, every constant function $u \in \mathcal{D}(\underline{E})$ is an exact solution.*

Proof If f is constant, then for an arbitrary u we have $c_1(u) = c_2(u) = f$ and $\mathcal{F}(u, f) = 0$. If f is not constant, for the data fidelity term $\mathcal{F}$ to vanish it must hold that

$$\int_\Omega (c_1(u) - f)^2 \, u \, \mathrm{d}x = 0$$

and

$$\int_\Omega (c_2(u) - f)^2 \, (1 - u) \, \mathrm{d}x = 0.$$

Let us define the sets $\Omega^+ := \{x \mid u(x) \in (0, 1]\}$ and $\Omega^- := \{x \mid u(x) \in [0, 1)\}$. We have that $\Omega^+ \cup \Omega^- = \Omega$, and if u is not binary we have $\Omega^+ \cap \Omega^- \neq \emptyset$. For $\mathcal{F}$ to be zero, it must hold that $f = c_1(u)$ on Ω^+ and $f = c_2(u)$ on Ω^-. Since the intersection of these sets is nonempty and the union is Ω we have that $c_1(u) = c_2(u) = f$ and f has to be constant. From that we conclude that u has to be binary and it is easy to see that a function u that is binary on the two constant regions of f satisfies $\mathcal{F}(u, f) = 0$. □

Note that there is no unique solution for which the fidelity term vanishes, since for an exact solution u^* the function $1 - u^*$ also represents an exact solution. In what follows we consider images consisting of K channels $f \in L^\infty(\Omega, [0, 1]^K)$, where each channel consists of a piecewise constant function taking only two values a_i^0 and a_i^1 for all $i = 1, \ldots, K$. We denote the sets $A_i^0 := \{x \in \Omega \mid f_i(x) = a_i^0\}$ and $A_i^1 := \{x \in \Omega \mid f_i(x) = a_i^1\}$.

Corollary 1 (Exact solution for $K \geq 2$) *Let $f^* \in L^\infty(\Omega, [0, 1]^K)$ be such that f_i^* is given as in Theorem 5 for $i = 1, \ldots, K$. Moreover, assume that at least one f^* is not constant a.e.. Then there exists a unique solution $u^* \in \mathcal{D}(\underline{E})$ fulfilling $\mathcal{F}(u^*, f^*) = 0$ if there exists $i \neq j$ and $(\alpha, \beta) \in \{0, 1\}^2$ such that $A_i^\alpha \cap A_j^\beta = \emptyset$.*

Proof Since $\mathcal{F}(u, f^*) = \mathcal{F}(u_1, f_1^*) + \mathcal{F}(u_2, f_2^*) + \cdots + \mathcal{F}(u_K, f_K^*)$ is simply the sum of K positive terms corresponding to single channel images, each of them has to vanish. We deduce from Theorem 5, that for this to be true each channel of u_i has to be binary on the constant regions of f_i. Therefore, if there exists $j \in \{1, \ldots, K\} \setminus \{i\}$ such that A_j^0 or A_j^1 does not overlap with A_i^0 or A_i^1, we can take the solutions with value 1 for u_i and u_j on these sets. Otherwise, if no such vector exists, there is a region where any solutions u_i and u_j are equal 1, and their sum in this region contradicts the conditions of the admissible set. □

In the following we investigate the convergence behaviour. Assuming that an exact solution of the fidelity term exists, i.e. that f^* satisfies the conditions of Corollary 1, we investigate the sensitivity of the solutions with respect to the images f. More precisely, convergence ensures that when $\lambda \to 0$ and $f^n \to f^*$, the solution u^n associated with f^n converges to a solution u of $\mathcal{F}(u, f^*) = 0$.

In the analysis so far, it has always been clear which image the mean values $c_{1,i}$ and $c_{2,i}$ refer to. This does not apply in the proof of Theorem 6 below, so we modify the notation for specifying the associated image on which the mean values are defined:
$c_{1,i}(u_i, f_i) := \frac{\int_\Omega f_i u_i \, \mathrm{d}x}{\int_\Omega u_i \, \mathrm{d}x}$ and $c_{2,i}(u_i, f_i) := \frac{\int_\Omega f_i (1 - u_i) \, \mathrm{d}x}{\int_\Omega (1 - u_i) \, \mathrm{d}x}$.

Theorem 6 (Convergence) *Let f^* be as given in Corollary 1, which implies the existence of a $u^* \in \mathcal{D}(\underline{E})$ such that $\mathcal{F}(u^*, f^*) = 0$. Assume that the f_i^* are constant on two sets with non-zero measure. Further let $(f^n)_{n \in \mathbb{N}}$ be noisy versions of f^* satisfying $\|f^* - f^n\|_\infty \leq \delta^n$ for a sequence $(\delta^n)_{n \in \mathbb{N}}$ converging to zero. Choosing the regularization parameter $\lambda : (0, \infty) \to (0, \infty)$ such that $\lambda^n := \lambda(\delta^n) \to 0$ for the sequence of minimizers defined by*

$$u^n := \arg\min_u \{\lambda^n \mathcal{R}(u) + \mathcal{F}(u, f^n)\}$$

it holds that $u^n \to u^*$.

Proof By the definition of u^n it follows that

$$\begin{aligned}
\mathcal{F}(u^n, f^n) + \lambda^n \mathcal{R}(u^n) &= \sum_{i=1}^K \int_\Omega (c_{1,i}(u_i^n, f_i^n) - f_i^n)^2 \, u_i^n \\
&\quad + \int_\Omega (c_{2,i}(u_i^n, f_i^n) - f_i^n)^2 \, (1 - u_i^n) + \lambda^n \mathcal{R}(u_i^n) \\
&\leq \sum_{i=1}^K \int_\Omega |c_{1,i}(u_i^*, f_i^n) - f_i^n| u_i^* \\
&\quad + \int_\Omega |c_{2,i}(u_i^*, f_i^n) - f_i^n| \, (1 - u_i^*) + \lambda^n \mathcal{R}(u_i^*) \\
&\leq \sum_{i=1}^K \int_\Omega (|c_{1,i}(u_i^*, f_i^n) - f_i^*| + |f_i^* - f_i^n|) \, u_i^* \\
&\quad + \int_\Omega (|c_{2,i}(u_i^*, f_i^n) - f_i^*| + |f_1^* - f_i^n|) \, (1 - u_i^*) \\
&\qquad + \lambda^n \mathcal{R}(u_i^*).
\end{aligned} \tag{17}$$

We estimate:

$$
\begin{aligned}
&|c_{1,i}(u_i^*, f_i^n) - f_i^*| + |f_i^* - f_i^n| \\
&= \left| \frac{\int_\Omega u_i^* (f_i^n - f_i^* + f_i^*)}{\int_\Omega u_i^*} - f_i^* \right| + |f_i^* - f_i^n| \\
&\leq |c_{1,i}(u_i^*, f_i^*) - f_i^*| + \left| \frac{\int_\Omega u_i^* |f_i^n - f_i^*|}{\int_\Omega u_i^*} \right| + |f_i^* - f_i^n|,
\end{aligned}
$$

and similarly we get

$$
\begin{aligned}
&|c_{2,i}(u_i^*, f_i^n) - f_i^*| + |f_i^* - f_i^n| \\
&\leq |c_{2,i}(u_i^*, f_i^*) - f_i^*| + \left| \frac{\int_\Omega (1 - u_i^*) |f_i^n - f_i^*|}{\int_\Omega (1 - u_i^*)} \right| \\
&\qquad + |f_i^* - f_i^n|.
\end{aligned}
$$

Inserting this into (17), using the fact that u^* is the exact solution of $\mathcal{F}(u, f^*) = 0$ and $\|f^* - f^n\|_\infty \leq \delta^n$, we obtain

$$
\begin{aligned}
\mathcal{F}(u^n, f^n) + \lambda^n \mathcal{R}(u^n) &\leq \sum_{i=1}^K \int_\Omega 2\delta^n u_i^* \\
&\quad + \int_\Omega 2\delta^n (1 - u_i^*) + \lambda^n \mathcal{R}(u_i^*) \longrightarrow 0.
\end{aligned} \tag{18}
$$

Further we know that

$$
\begin{aligned}
&\mathcal{F}(u^n, f^*) + \lambda^n \mathcal{R}(u^n) \\
&\quad = \sum_{i=1}^K \int_\Omega \left(c_{1,i}(u_i^n, f_i^*) - f_i^*\right)^2 u_i^n \\
&\quad + \int_\Omega \left(c_{2,i}(u_i^n, f_i^*) - f_i^*\right)^2 (1 - u_i^n) + \lambda^n \mathcal{R}(u_i^n) \\
&\quad \leq \sum_{i=1}^K \int_\Omega |c_{1,i}(u_i^n, f_i^n) - f_i^*| \, u_i^n \\
&\quad + \int_\Omega |c_{2,i}(u_i^n, f_i^n) - f_i^*| \, (1 - u_i^n) + \lambda^n \mathcal{R}(u_i^n).
\end{aligned}
$$

Using the triangle inequality we conclude that

$$
\begin{aligned}
\mathcal{F}(u^n, f^*) &\leq \sum_{i=1}^K \int_\Omega \left(|c_{1,i}(u_i^n, f_i^n) - f_i^n| + |f_i^n - f_i^n|\right) u_i^n \\
&\quad + \int_\Omega \left(|c_{2,i}(u_i^n, f_i^n) - f_i^n| + |f_i^n - f_i^*|\right) (1 - u_i^n) \\
&\leq \sum_{i=1}^K \int_\Omega \left(|c_{1,i}(u_i^n, f_i^n) - f_i^n| + \delta^n\right) u_i^n \\
&\quad + \int_\Omega \left(|c_{2,i}(u_i^n, f_i^n) - f_i^n| + \delta^n\right) (1 - u_i^n) \\
&= \mathcal{F}(u^n, f^n) + \delta^n K |\Omega|.
\end{aligned}
$$

Combined with inequality (18) we obtain that $\mathcal{F}(u^n, f^*) \to 0$. Since the bound on $\underline{E}(u^n, f^*)$ in (11) is independent of u^n, the sequence u^n is bounded in $BV(\Omega)$, and therefore up to extraction it converges.

Since f^* is constant on a set with non-zero measure, we know that for n large enough, f^n is non-zero on a set with non-zero measure as well. This implies that the minimizers u^n are not binary on the whole domain Ω. Additionally, as $\mathcal{F}$ is continuous with respect to u, except for $u = 1$ and $u = 0$, we get that $\lim_{n\to\infty} \mathcal{F}(u^n, f^*) = \mathcal{F}(u^*, f^*) = 0$, which concludes the proof. □

5 Numerical Implementation

In this section we present details of the numerical implementation of the proposed method. First we introduce the discrete setting which will be used throughout the rest of this section. Next, the employed optimization procedure is described.

5.1 Discrete Setting

Let us fix our main notation which are similar to those used in [7,8]. To simplify, our images will be two-dimensional matrices of size $M \times N$. We therefore consider the set of indices of the image domain

$$\{(jh, kh) : 1 \leq j \leq M, 1 \leq k \leq N\},$$

where h denotes the grid step size and (j, k) are the indices of the nodes (jh, kh) in the image domain. Let $X = \mathbb{R}^{M \times N}$ be a finite dimensional vector space equipped with the scalar product

$$\langle u, v \rangle_X = \sum_{j,k} u_{j,k} v_{j,k}, \quad u, v \in X.$$

The vector field ∇u has values in $Y = X \times X$. For discretization of $\nabla : X \to Y$, we use standard finite differences with Neumann boundary conditions

$$(\nabla u)_{j,k} = \begin{pmatrix} (\nabla u)^1_{j,k} \\ (\nabla u)^2_{j,k} \end{pmatrix},$$

where

$$(\nabla u)^1_{j,k} = \begin{cases} \frac{u_{j+1,k} - u_{j,k}}{h} & \text{if } j < M, \\ 0 & \text{if } j = M, \end{cases}$$

$$(\nabla u)^2_{j,k} = \begin{cases} \frac{u_{j,k+1} - u_{j,k}}{h} & \text{if } k < N, \\ 0 & \text{if } k = N. \end{cases}$$

We also define in Y the scalar product

$$\langle p, q \rangle_Y = \sum_{j,k} p^1_{j,k} q^1_{j,k} + p^2_{j,k} q^2_{j,k},$$

where $p = (p^1, p^2), q = (q^1, q^2) \in Y$.

Furthermore we also need the discrete divergence operator $\operatorname{div} p : Y \to X$, which is chosen to be adjoint to the discrete gradient operator. In particular, one has $-\operatorname{div} = \nabla^*$ which is defined through the identity

$$\langle \nabla u, p\rangle_Y = -\langle u, \operatorname{div} p\rangle_X.$$

The discrete version of the isotropic total variation norm is defined as

$$\|\nabla u\|_1 = \sum_{j,k} |(\nabla u)_{j,k}|$$
$$\text{where } |(\nabla u)_{j,k}| = \sqrt{\left((\nabla u)^1_{j,k}\right)^2 + \left((\nabla u)^2_{j,k}\right)^2},$$

and the discrete maximum norm for some element $p \in Y$ is given as

$$\|p\|_\infty = \max_{j,k} \sqrt{(p^1_{j,k})^2 + (p^2_{j,k})^2}.$$

Using the discrete setting given above, the discrete form of the proposed model is then given by

$$\min_{(u_i)_{i=1}^K} \sum_{i=1}^K \left[\lambda \|\nabla u_i\|_1 + \|F_1(u_i)\|_1 + \|F_2(u_i)\|_1\right]$$
$$\text{subject to} \qquad (19)$$
$$1) \sum_{i=1}^K (u_i)_{j,k} \le 1, \quad 2)\ 0 \le (u_i)_{j,k},\ i = 1,\dots,K$$
$$j = 1,\dots,M,\ k = 1,\dots,N,$$

where $(f_i)_{i=1}^K$ is the given image with K channels and $(u_i)_{i=1}^K \in X^K$ the sought solution, representing the assignment of each pixel to the labels. More precisely, the fidelity terms $F_1, F_2 : X \to X$ in (19) are given by

$$\big(F_1(u_i)\big)_{j,k} = \big(c_1(u_i) - (f_i)_{j,k}\big)^2 \cdot (u_i)_{j,k}$$
$$\big(F_2(u_i)\big)_{j,k} = \big(c_2(u_i) - (f_i)_{j,k}\big)^2 \cdot \big(1 - (u_i)_{j,k}\big),$$

for $i = 1,\dots,K$ and

$$c_1(u_i) = \frac{\langle u_i, f_i\rangle_X}{\|u_i\|_1} \text{ and } c_2(u_i) = \frac{\langle \mathbb{1} - u_i, f_i\rangle_X}{\|\mathbb{1} - u_i\|_1}, \qquad (20)$$

where $\mathbb{1}$ denotes the all-ones matrix of size $M \times N$. It is well known that variational methods incorporating total variation regularization present difficulties due to the lack of smoothness. We therefore apply a flexible algorithm proposed in [8], that is particularly suitable for non-smooth optimization problems like (19).

5.2 Primal Dual Optimization Scheme

Minimization problems of the type (19) constitute a large scale optimization problem which are traditionally addressed using gradient based methods such as gradient descent. The latter requires smoothness of the functional for guaranteeing convergence, that we do not have. Therefore, we opt for the optimization scheme proposed in [8]. For this purpose, we reformulate the functional of (19) in a form that is more suitable for the minimization method we apply in this work:

$$\min_{(u_i)_{i=1}^K} \sum_{i=1}^K \mathcal{F}\big(\mathcal{K}(u_i)\big) + \mathcal{G}(u). \qquad (21)$$

One method to minimize non-smooth objective functionals consists in using the proximal point algorithm. For a convex objective functional $\mathcal{E} : X \to \mathbb{R}$, the proximal step replaces the traditional gradient step, as follows

$$u_{k+1} = \operatorname{prox}_{\tau\mathcal{E}}(u_k)$$

where $\tau \in \mathbb{R}^+$ is a step size and the proximal operator is defined by

$$\operatorname{prox}_{\tau\mathcal{E}}(u) = \operatorname*{arg\,min}_{u' \in X} \left(\mathcal{E}(u') + \frac{1}{2\tau}\|u' - u\|_X^2\right). \qquad (22)$$

This algorithm is rarely applied for solving (19), since in general (22) does not have a closed form solution. Proximal primal-dual schemes are rather used. In these algorithms, an auxiliary dual variable chosen in the range of the operator is introduced, and the primal ($u \in X$) and dual variables are alternately updated. One possible primal-dual scheme is the so-called primal dual hybrid gradient (PDHG) algorithm [8], also known as the Chambolle-Pock algorithm, with a recent extension to nonlinear operators in [31], where the authors study the solution of saddle-point problems of the form

$$\min_{u\in X} \max_{p\in Z} \langle \mathcal{K}(u), p\rangle + \mathcal{G}(u) - \mathcal{F}^*(p),$$

in finite-dimensional Hilbert spaces X and Z. The functions $\mathcal{G} : X \to [0, +\infty]$ and $\mathcal{F}^* : Z \to [0, +\infty]$ are assumed to be proper, convex, lower semi-continuous (l.s.c), $\mathcal{F}^*$ being itself the convex conjugate of a convex l.s.c. function $\mathcal{F}$. The saddle-point problem is a primal-dual formulation of the nonlinear primal problem formulated in (21). For more details we refer to the literature [8] and [29].

The PDHG method can be applied to solve problem (19), but since the proximals of $\|\nabla u_i\|_1, \|F_1(u_i)\|_1$

and $\|F_2(u_i)\|_1$ are difficult to compute, we use the following identification in order to recast (19) into (21):

$$\begin{aligned} \mathcal{K}(u_i) &:= [\nabla u_i, F_1(u_i), F_2(u_i)], \\ \mathcal{F}(p_i^{(1)}, p_i^{(2)}, p_i^{(3)}) &:= \lambda\|p_i^{(1)}\|_1 + \|p_i^{(2)}\|_1 + \|p_i^{(3)}\|_1, \\ \mathcal{G}(u) &:= i_U(u), \end{aligned} \quad (23)$$

where $\mathcal{K} : X \to Z$ with $Z = Y \times X \times X$ and $\mathcal{F} : Z \to [0, +\infty]$, and where i_C denotes the indicator function of a convex set C, namely

$$i_C(u) = \begin{cases} 0, & \text{if } u \in C, \\ +\infty, & \text{if } u \notin C. \end{cases}$$

In (23), $\mathcal{K}$ is nonlinear because of $F_1(u_i)$ and $F_2(u_i)$. Since U is a convex set, the functionals $\mathcal{F}$ and $\mathcal{G}$ are convex.

We summarize in Algorithm 1 the PDHG algorithm adapted for minimization problems of the form (21), with possible nonlinear operator $\mathcal{K}$. In order to guarantee convergence, the step size is bounded by $\|K\|$, where

$$\|\mathcal{K}\| = \max\{\|\mathcal{K}u\|_2 \mid u \in X,\ \|u\|_2 \le 1\}.$$

In Algorithm 1 the term $[\partial\mathcal{K}(u^n)]^* : Z \to X$ denotes the adjoint of the derivative of $\mathcal{K}$ at point u^n. In the next section we illustrate the applicability of the primal dual algorithm to Problem (8).

Algorithm 1: Nonlinear primal dual gradient

Given: $\sigma, \tau > 0$, such that $\sigma\tau\|\mathcal{K}\|^2 < 1, \theta \in [0, 1]$ and $u^0, \bar{u}^0 \in X, p^0 \in Z$;
for $n = 0, \dots$ **do**
  $h^{n+1} \leftarrow \text{prox}_{\sigma\mathcal{F}^*}\left(p^n + \sigma\mathcal{K}(\bar{u}^n)\right)$;
  $u^{n+1} \leftarrow \text{prox}_{\tau\mathcal{G}}(u^n - \tau[\partial\mathcal{K}(u^n)]^*(h^{n+1}))$;
  $\bar{u}^{n+1} \leftarrow u^{n+1} + \theta(u^{n+1} - u^n)$
end

5.3 Application of the Chambolle-Pock algorithm to the proposed model

The two constraints of the minimization problem (19) force the solution to stay in the unit simplex U, defined as follows

$$U = \Big\{u \in X^K \mid (u_i)_{j,k} \ge 0,\ \forall 1 \le i \le K, \\ \sum_{i=1}^{K}(u_i)_{j,k} \le 1,\ \forall 1 \le j \le M,\ 1 \le k \le N\Big\}.$$

Dealing with (23), the computations of proximal operators, Fenchel conjugate and differential, required in Algorithm 1, are given below.

Let us start with the computation of the proximal operators $\text{prox}_{\sigma\mathcal{F}^*}$ and $\text{prox}_{\tau\mathcal{G}}$. The Fenchel conjugate of $\|\cdot\|_1$ is the indicator function of the unit ball of the dual norm: For $p \in X$, we have $\|p\|_1^* = i_P(p)$, where $P = \{p \in X \mid \|p\|_\infty \le 1\}$. For $p \in Y$, it holds that $(\lambda\|p\|_1)^* = i_{\tilde{P}}(p)$, where $\tilde{P} = \{p \in Y \mid \|p\|_\infty \le \lambda\}$. In both cases, the proximal operators with respect to this function can be easily evaluated. More precisely, it holds that

$$\text{prox}_{i_P}\big([p_i^{(1)}, p_i^{(2)}, p_i^{(3)}]\big) = \\ \big(\text{prox}_{i_{\tilde{P}}}(p_i^{(1)}), \text{prox}_{i_P}(p_i^{(2)}), \text{prox}_{i_P}(p_i^{(3)})\big), \quad (24)$$

since in our case we have $p^{(1)} \in Y$ and $p^{(2)}, p^{(3)} \in X$. As the proximal operator of a convex set reduces to pointwise Euclidean projectors onto L^2 balls, we obtain

$$\Big(\text{prox}_{i_P}(p_i^{(l)})\Big)_{j,k} = \frac{(p_i^{(l)})_{j,k}}{\max\{1, |(p_i^{(l)})_{j,k}|\}},$$

for $l \in \{2, 3\}$. In (24), the corresponding proximal operator of the projection onto $\tilde{P}$ looks as follows

$$\Big(\text{prox}_{i_{\tilde{P}}}(p_i^{(1)})\Big)_{j,k} = \begin{bmatrix} \frac{(p_{i1}^{(1)})_{j,k}}{\max\{\lambda, |(p_{i1}^{(1)})_{j,k}|\}} \\ \frac{(p_{i2}^{(1)})_{j,k}}{\max\{\lambda, |(p_{i2}^{(1)})_{j,k}|\}} \end{bmatrix}.$$

The proximal operator with respect to $\mathcal{G}$ is the orthogonal projector onto the unit simplex U. It is known that this projection can be computed with a finite number of steps. We therefore apply the algorithm proposed in [22] and denote the resulting projection by prox_{i_U}. Since the discrete total variation operator is linear, the adjoint of the derivative is, as already stated in Section 5.1, its adjoint, i.e.

$$\langle \nabla u_i, p_i \rangle = -\langle u_i, \operatorname{div} p_i \rangle.$$

Due to its non-differentiability, we replace the ℓ^1-norm present in $c_1(u_i)$ and $c_2(u_i)$ in (20), by a differentiable approximation. In particular, we consider the approximation defined by Lee et al. in [20], that replaces the ℓ^1-norm by the function

$$\|u_i\|_\epsilon = \sum_{j,k} \sqrt{\big((u_i)_{j,k}\big)^2 + \epsilon}.$$

This function is twice Fréchet-differentiable, and $\lim_{\epsilon \to 0^+} \|u_i\|_\epsilon = \|u_i\|_1$.

Remark 1 Note that, even if $\|\cdot\|_\epsilon$ is smooth, the convergence quality of a standard gradient descent method in this context would depend on to the condition number of the underlying Hessian matrix, which is inversely proportional to ϵ, and therefore such a direct approach would not be relevant.

We linearize the nonlinear terms F_1 and F_2 in (20) by computing their derivatives $\frac{\partial}{\partial u_i}F_1(u_i)$ and $\frac{\partial}{\partial u_i}F_2(u_i)$, and next the corresponding adjoints. For the sake of simplicity, we describe $u_i \in X$ and $f_i \in X$ as vectors, i.e.

$$\tilde{u}_i \coloneqq \begin{bmatrix} (u_i)_1 \\ \vdots \\ (u_i)_{\tilde{N}} \end{bmatrix}, \quad \tilde{f}_i \coloneqq \begin{bmatrix} (f_i)_1 \\ \vdots \\ (f_i)_{\tilde{N}} \end{bmatrix},$$

where $\tilde{u}_i, \tilde{f}_i \in \mathbb{R}^{\tilde{N}}$, with $\tilde{N} = MN$. We further denote by $e_k \in \mathbb{R}^{\tilde{N}}$ the k-th vector of the canonical basis, and by $\mathrm{I}_{\tilde{\mathrm{N}}} \in \mathbb{R}^{\tilde{N}\times\tilde{N}}$ the identity matrix.

The derivatives of the fidelity terms $F_1(u_i)$ and $F_2(u_i)$ can be determined in a rather simple way and formulated in closed form as follows

$$\frac{\partial}{\partial u_i}F_1(u_i) = T_i^2 - 2T_iQ_iU_i, \tag{25}$$

where T_i and U_i are diagonal matrices of dimension $\tilde{N}\times\tilde{N}$ and are given by

$$T_i \coloneqq \sum_{k=1}^{\tilde{N}} \tilde{f}_i e_k^T - \frac{\langle u_i, f_i\rangle}{\|u_i\|_\epsilon}\mathrm{I}_{\tilde{\mathrm{N}}}, \quad U_i \coloneqq \sum_{k=1}^{\tilde{N}} \tilde{u}_i e_k^T.$$

The matrix Q_i is dense and given by

$$Q_i \coloneqq \begin{bmatrix} \frac{(\tilde{f}_i)_1\|u_i\|_\epsilon - \frac{(\tilde{u}_i)_1}{\sqrt{(\tilde{u}_i)_j^2+\epsilon}}\langle u_i, f_i\rangle}{\|u_i\|_\epsilon^2} \\ \vdots \\ \frac{(\tilde{f}_i)_{\tilde{N}}\|u_i\|_\epsilon - \frac{(\tilde{u}_i)_1}{\sqrt{(\tilde{u}_i)_{\tilde{N}}^2+\epsilon}}\langle u_i, f_i\rangle}{\|u_i\|_\epsilon^2} \end{bmatrix} \otimes \mathbb{1}_{\tilde{N}}^T,$$

where $\otimes$ is the Kronecker product, and $\mathbb{1}_{\tilde{N}}$ denotes the all-ones column of length $\tilde{N}$. Since diagonal matrices are self-adjoint and the adjoint of a real-valued matrix is simply its transpose, the adjoint of (25) is given by

$$\left[\frac{\partial}{\partial u_i}F_1\big((u_i)\big)\right]^* = T_i^2 - 2U_iQ_i^TT_i.$$

The adjoint of the derivative of $F_2(u_i)$ is expressed in the same manner as in (25). We have

$$\frac{\partial}{\partial u_i}F_2(u_i) = S_i^2 - 2S_iR_iV_i,$$

and

$$\left[\frac{\partial}{\partial u_i}F_2\big((u_i)\big)\right]^* = S_i^2 - 2V_iR_i^TS_i,$$

where we introduced the following diagonal matrices

$$S_i \coloneqq \sum_{k=1}^{\tilde{N}} \tilde{f}_i e_k^T - \frac{\langle \mathbb{1}-u_i, f_i\rangle}{\|\mathbb{1}-u_i\|_\epsilon}\mathrm{I}_{\tilde{\mathrm{N}}}, \quad V_i \coloneqq \mathrm{I}_{\tilde{\mathrm{N}}} - \sum_{k=1}^{\tilde{N}} \tilde{u}_i e_k^T$$

and the following dense matrix

$$R_i \coloneqq \begin{bmatrix} \frac{(\tilde{f}_i)_1\|\mathbb{1}-u_i\|_\epsilon + \frac{1-(\tilde{u}_i)_1}{\sqrt{(1-(\tilde{u}_i)_i)_1^2+\epsilon}}\langle \mathbb{1}-u_i, f_i\rangle}{\|\mathbb{1}-u_i\|_\epsilon^2} \\ \vdots \\ \frac{(\tilde{f}_i)_{\tilde{N}}\|\mathbb{1}-u_i\|_\epsilon + \frac{1-(\tilde{u}_i)_{\tilde{N}}}{\sqrt{(1-(\tilde{u}_i)_{\tilde{N}})^2+\epsilon}}\langle \mathbb{1}-u_i, f_i\rangle}{\|\mathbb{1}-u_i\|_\epsilon^2} \end{bmatrix} \otimes \mathbb{1}_{\tilde{N}}^T.$$

In order to obtain an upper bound for the step size τ and θ, we have to compute $\|\mathcal{K}\|$, which is straightforward (see [7] for the computation of $\|\operatorname{div} p\|$) and gives $\|\mathcal{K}\| \leq \sqrt{10}$. We initialize u_i by $\widehat{f}_i$, the normalized version of f_i, such that the constraints given in (19) are satisfied. Thus, all the quantities used in Algorithm 2 have been defined.

Algorithm 2: Nonlinear primal dual gradient to solve Problem (19)

Given: $\sigma, \tau > 0$, such that $\sigma\tau\|\mathcal{K}\|^2 < 1$, $\theta \in [0,1]$ and $f \in X^K$;
Initialization: $p_i^{(1)} \in Y, p_i^{(2)}, p_i^{(3)} \in X$, $f_i, u_i^0 \leftarrow \widehat{f}_i$;
for $n = 0, \dots$ **do**
  for $i = 1, \dots, K$ **do**
    $p_{i1}^{(1)n+1} \leftarrow \big(p_{i1}^{(1)n} + \sigma\nabla u_i^n\big)/\max\{\lambda\mathbf{1}, |p_i^{(1)n} + \sigma\nabla u_i^n|_2\}$;
    $p_{i2}^{(1)n+1} \leftarrow \big(p_{i2}^{(1)n} + \sigma\nabla u_i^n\big)/\max\{\lambda\mathbf{1}, |p_i^{(1)n} + \sigma\nabla u_i^n|_2\}$;
    $p_i^{(2)n+1} \leftarrow \big(p_i^{(2)n} + \sigma\nabla u_i^n\big)/\max\{\mathbf{1}, |p_i^{(2)n} + \sigma F_1(u_i^n)|_2\}$;
    $p_i^{(3)n+1} \leftarrow \big(p_i^{(3)n} + \sigma\nabla u_i^n\big)/\max\{\mathbf{1}, |p_i^{(3)n} + \sigma F_2(u_i^n)|_2\}$;
  end
  $f^{n+1} \leftarrow \operatorname{prox}_{i_U}\Big(f^n + \tau\operatorname{div} p^{(1)n+1} - \tau\Big[\partial F_1\Big(u^n\Big)\Big]^* p^{(2)n+1} - \tau\Big[\partial F_2(u^n)\Big]^* p^{(3)n+1}\Big)$;
  $u^{n+1} \leftarrow f^{n+1} + \theta(f^{n+1} - f^n)$;
end

6 Experimental Results

In this section we present several experiments demonstrating the possible applicability of the proposed segmentation framework to artificial and medical images. We compare our results with those obtained by channel-wise application of the level-set method proposed by Chan and Vese in [10], its convex relaxation [9] and with the multichannel multiphase method [32], each of them introduced in Section 2.1.

We start with two examples illustrating the statement of Corollary 1. Figure 1 serves as an example for an image consisting of two channels, with non-overlapping regions and corresponding minimizers. Figure 2 depicts

the evolution of the energy functional during the optimization process, which shows that in this example no regularization is required and the solution u^* to $\mathcal{F}(u, f) = 0$ exists and is unique.

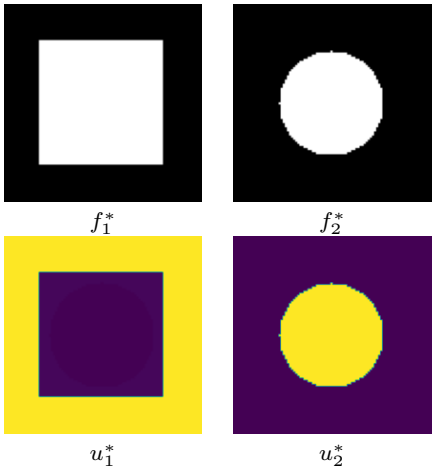

Fig. 1: Representation of the unique, exact solution of $\mathcal{F}(u, f^*) = 0$, where f^* consists of two channels denoted by f_1^* and f_2^*. In this example, the white circle can be understood as A_1^0, while A_2^0 is the white square and thus the proper subset relation is fulfilled.

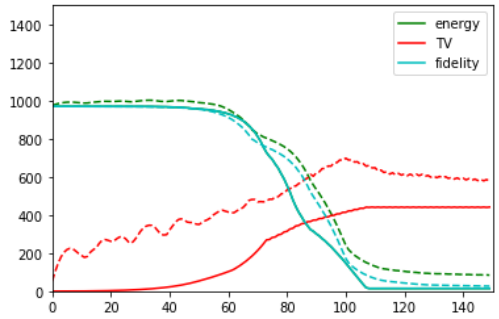

Fig. 2: Evolution of energy, TV and fidelity corresponding to the segmentation problem depicted in Figure 1. The solid line shows the evolution of the non-regularized problem ($\lambda = 0$), while the dashed line presents the results acquired by setting $\lambda = 0.1$.

Figure 4 shows the evolution of data fidelity and total variation corresponding to the minimization of $\mathcal{F}(u, f)$ with f as depicted in Figure 3. The solid and dashed lines correspond to two different initializations of the algorithm. In the first case, u^0 (see Algorithm 2) is chosen to be constant with a value of 0.3 and in the second case u^0 is f. This example confirms what is shown in the proof of Corollary 1, namely that for $K \geq 2$, where the images consist of regions that overlap channelwise, there is no $u \in \mathcal{D}(\underline{\mathrm{E}})$ fulfilling $\mathcal{F}(u, f) = 0$. The corresponding curves depicting evolution of fidelity and TV for different initializations, are presented in

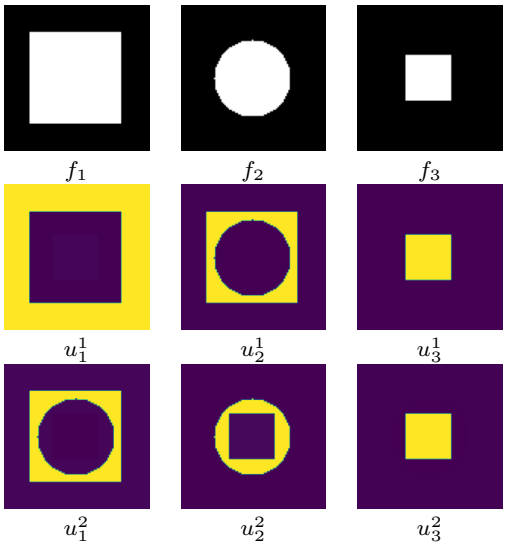

Fig. 3: Visualization of the minimizers of fidelity $\mathcal{F}$ found in the overlapping three-channel case. No exact and unique solution can be found. The two solutions, u^1 and u^2, result from different initializations.

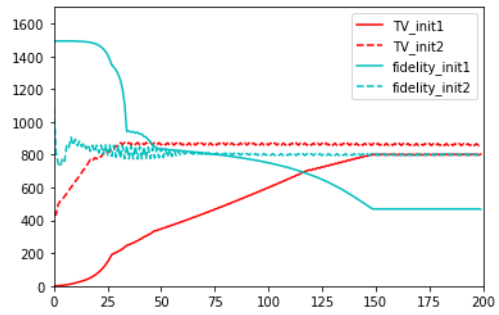

Fig. 4: Evolution of fidelity and TV for two different initializitations corresponding to the results shown in Figure 3. More precisely, the dashed line corresponds to the minimizers u in the second row and the solid line to those in the bottom row.

Figure 4. In both cases, there is no regularization (i.e. $\lambda = 0$) and a local minimum of the data term $\mathcal{F}$ is obtained.

6.1 Extraction of Feature Maps

The first step of our segmentation framework is the extraction of feature maps. For this purpose, we choose suitable filtering methods to separate certain objects of an image from the background. This is achieved by using color filters, Gabor filters [17] and simple windowing techniques, depending on the properties of the image f. As our forthcoming experiments will show, this pre-filtering is often not required for medical images, as the different channels originate from different medical imaging techniques.

6.1.1 Texture Segmentation

Texture is an important property of surfaces which characterizes their nature. Texture segmentation is the process of partitioning an image into regions based on their texture. In [15] the authors demonstrate a multichannel approach to the texture segmentation problem. Inspired by the human visual system (HVS), they propose a multi-channel filtering approach to tune multiple filters with different spatial frequencies and orientations to capture important texture information through separate channels. To this end, the authors use Gabor filters, a special class of bandpass filters that can be viewed as a sinusoidal signal with a specific frequency and orientation modulated by a Gaussian wave. They are particularly useful for texture segmentation problems, as they have optimal localization properties in both the spatial and frequency domains. By carefully designing a Gabor filter bank covering the spatial-frequency domain, they decompose an image into multi-resolutions that correspond to different texture characteristics. The final step of their unsupervised texture segmentation approach is the clustering of pixels into a number of clusters representing the original texture regions. For that purpose the authors employ basic K-means clustering algorithm. Inspired by their work, we also apply Gabor filters in order to extract feature maps $f_1, \dots, f_K$ of textured parts of f, which serve as input of the proposed multi-channel energy functional.

in Figure 5 a first example of the extraction of a feature map is demonstrated by applying Gabor filters to an image containing texture. The resulting feature map is then further processed by solving the minimization problem (19), and compared with the segmentation of the input image without previous feature extraction. This example illustrates the importance of the pre-filtering process.

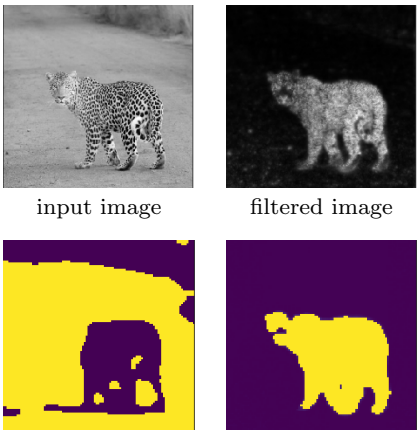

Fig. 5: The first row of this figure shows the input image containing texture and corresponding extracted feature map representing a linear combination of Gabor filtered images. In the bottom row a comparison of segmentation of raw input and filtered image, is depicted. This example highlights the utility of the pre-filtering process in texture-based segmentation.

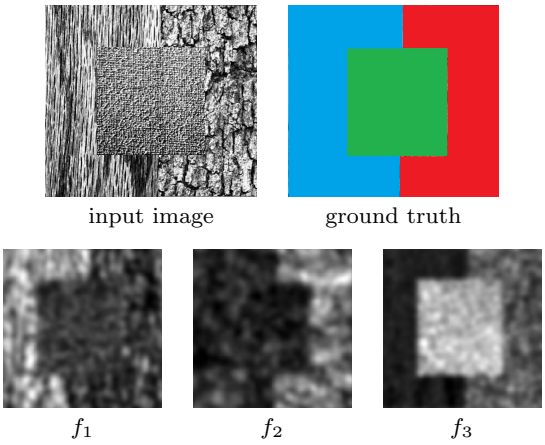

Fig. 6: The first row shows the three-texture Brodatz input image and the sought-after solution. In the second row the via Gabor filtering obtained extracted feature maps are depicted. Overlapping regions are clearly visible.

Figure 6 shows an artificial texture image consisting of three different Brodatz textures and the corresponding ground truth segmentation, as well as the feature maps extracted via Gabor filtering, representing the three channels f_1, f_2 and f_3 in the minimization problem formulated in (19). In Figure 7 the minimizers of the energy functional for different regularization parameters λ are presented. It is worth mentioning that here, we heuristically test which λ is most suitable for the present problem. A detailed analysis of the choice of λ would be of interest, but such an analysis is beyond the scope of this article, yet could be part of a future planned work. This example highlights the role of the regularization parameter and the results give rise to the assumption that moderate values of λ lead to more accurate results. In Figure 8 we show the evolution of energy, TV and the absolute error compared with the ground truth depicted in Figure 6, depending on different values of the regularization parameter λ. The curves confirm what the segmentation results in Figure 7 suggest, namely that a moderate value of the regularization parameter ($\lambda = 0.5$) lead to lower values of energy and absolute error. In this concrete example, the choice of a rather large regularization parameter seems to be appropriate, which can be justified by the "holes" in the extracted feature maps (see Figure 6).

The proposed method can also be applied to RGB images as demonstrated in Figure 9, where the input image is an RGB image of size 250×250. By prefiltering via Gabor filters and the use of a color filter, the two feature maps f_1 and f_2 depicted in Figure 9 are ob-

Fig. 7: Results for different values of the regularization parameter λ corresponding to the segmentation problem depicted in Figure 6. Holes in the segmentation mask disappear by enlarging the regularization parameter.

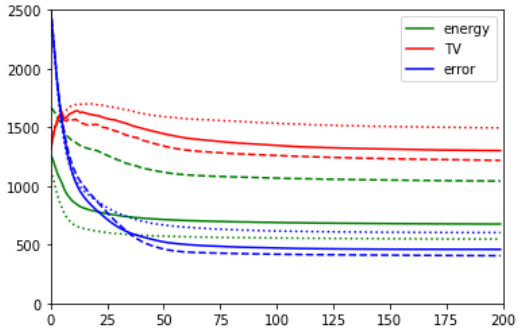

Fig. 8: Evolution of TV, energy and absolute error over 200 iterations when computing the segmentation depicted in Figure 7 for $\lambda = 0.1$ (dotted), $\lambda = 0.2$ (solid) and $\lambda = 0.5$ (dashed).

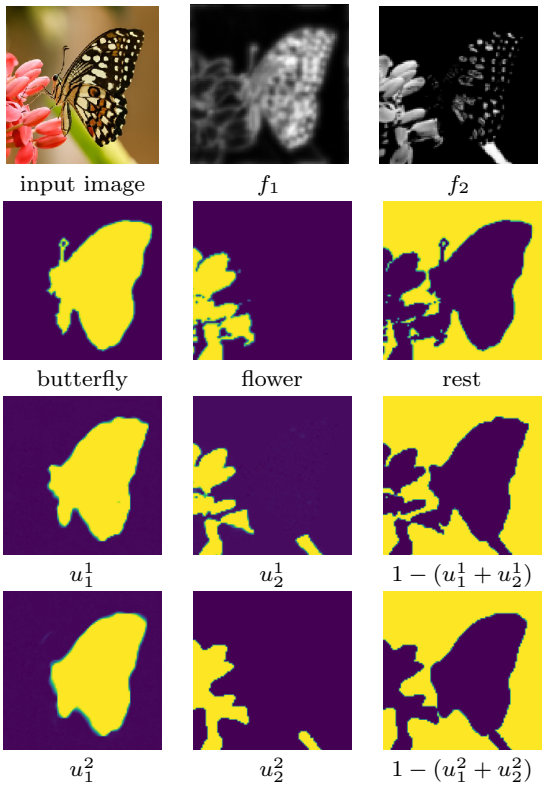

Fig. 9: The first row shows the input image and extracted feature maps via Gabor filtering and color filtering, respectively. Overlapping regions are clearly visible. In the second row the ground truth binary masks are depicted. The last two rows show the minimizers of problem (19), u_1 and u_2, and the remaining rest class with regularization parameter $\lambda = 0.1$ and $\lambda = 0.5$.

tained. It is clearly visible that the two images, which serve as input channels, contain undesired overlapping regions. In the bottom row of Figure 9, the minimizers of the proposed energy are presented. The set of unlabeled pixels which result from the formulation of the first constraint in (19) is summarized as background class. In Figure 10 the development of energy, TV and fidelity term as well as the absolute error are depicted. The curves correspond to two different values of the regularization parameter λ, and as confirmed by the results in Figure 9, a smaller value of λ (0.1) leads to a better result as more details in the contours of the objects are preserved.

We further demonstrate the applicability of our method to more complex problems, such as the one shown in Figure 11. In this example, the number of input images $K = 5$ and the feature maps are again obtained by application of Gabor filters and simple thresholding. The pre-filtered images slightly highlight the five different texture regions, but again there are many overlaps and "holes". The minimizer of energy (6) is depicted in Figure 12, where furthermore the results are compared to those obtained by minimizing the active contour model [10] and the convex relaxation of the active contour model [9] for each channel separately. This example shows the importance of the constraint preventing the results from overlapping. Operating on

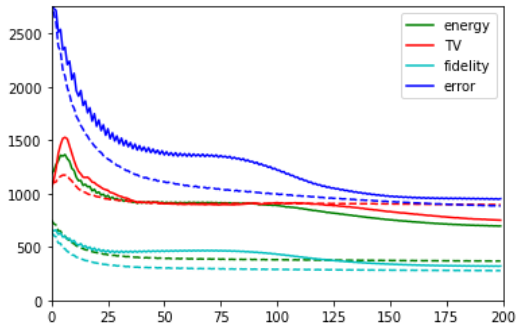

Fig. 10: Evolution of fidelity, TV, energy and absolute error over 200 iterations when computing the segmentation depicted in Figure 9 for $\lambda = 0.1$ (dashed) and $\lambda = 0.5$ (solid). In this example a smaller value of λ leads to slightly better results, which is also confirmed by the results depicted in Figure 9.

each channel individually leads to unsatisfactory results as can be observed from third and bottom row in Figure 12.

The example in Figure 13 demonstrates that our method can also compete with the multichannel multiphase (MMCV) approach proposed by Chan and Vese in [32]. We applied the algorithm implemented in MATLAB by Yue Wu [33]. In this example, the input f is

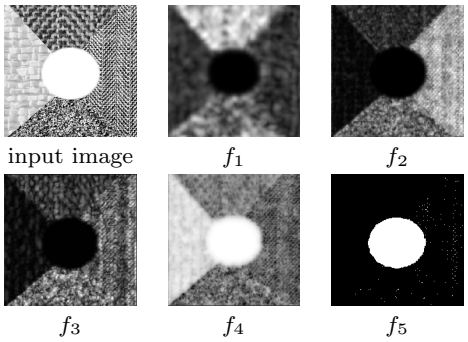

Fig. 11: Input texture image and the five extracted feature maps via gabor filtering and thresholding. The clearly visible overlapping regions were successfully removed from the proposed energy functional (see Figure 12).

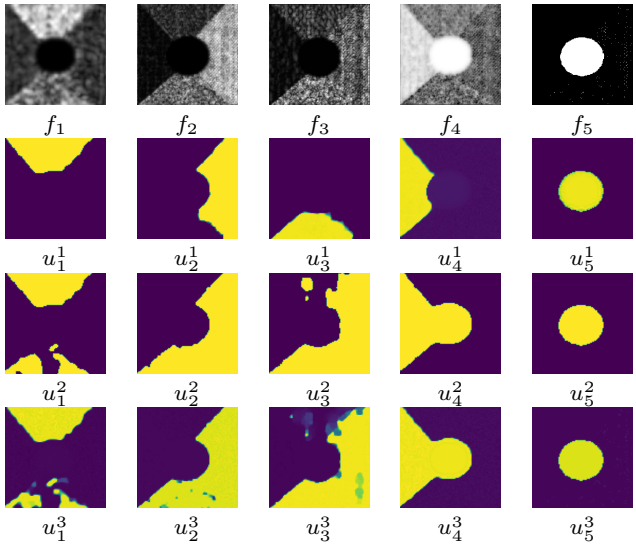

Fig. 12: The top row shows the minimizers u of the proposed energy functional, in the middle row the results achieved by the active contour model [10] method are depicted and the bottom row shows the results acquired by minimizing the convex relaxation of the Chan Vese model [9] for each channel separately. The experiment was carried out using a regularization parameter λ of 0.1.

an RGB image, so we have three channels serving as input images of the proposed method. Both methods achieve acceptable results, although those of the proposed method look slightly smoother.

6.2 Application to Medical Images

Our proposed method is applied to medical images where the different channels naturally result from different imaging techniques. Our multichannel multiphase functional uses the information contained in the different categories of MRI and CT images or images resulting from different modalities, and can therefore divide the input image naturally into K non-overlapping subregions.

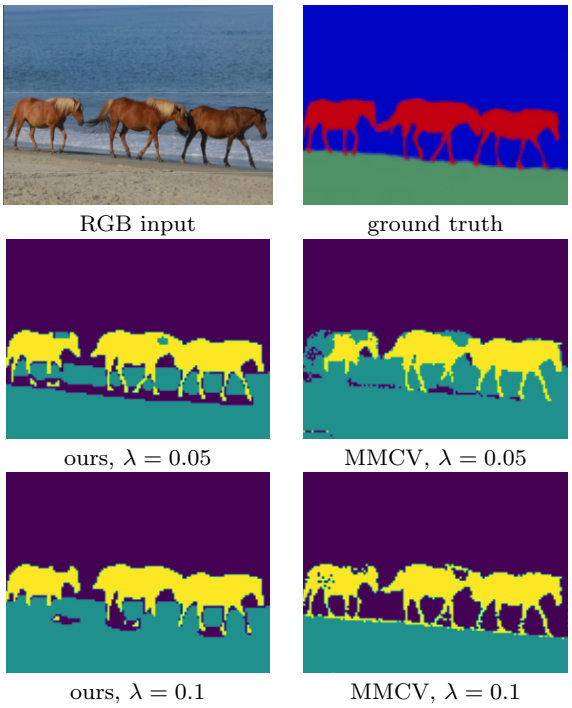

Fig. 13: Comparison of the segmentation of an RGB image obtained by the present method (left column) with the one obtained by the multichannel multiphase approach proposed by Chan and Vese in [32] corresponding to two different values of the regularization parameter λ.

As a first example, we illustrate the application of presented method in the neuroradiological field by dividing MRI images showing an abscess into the regions "healthy", "abscess" and "edema". In Figure 14, the top row depicts the MRI images, more specifically, DWI (diffusion weighted imaging), ADC (apparaent diffusion coefficient) and T2 sequence. As preprocessing, the ADC maps and T2 images were windowed and standardized to have intensity values between $[0, 1]$. This naturally highlights the regions to be distinguished. Thus, f_1, f_2 and f_3 are directly given. The remaining rows of Figure 14 show the minimizers u_1^j, u_2^j and u_3^j, $j \in \{1, \ldots, 4\}$, corresponding to the four different regularization parameters which were applied. Smaller values of λ result in quite inaccurate results contianing many false positives. The results in the last row, which were obtained by setting the regularization parameter to $\lambda = 0.2$, show an improvement compared to the ones in the previous rows.

We conduct a second experiment on the BRATS (Brain Tumor Segmentation) Challenge 2015[1] dataset (Figure 15). Each channel contains different information and is necessary for accurate diagnosis and quantification of tumor growth. More precisely, in Figure 15,

[1] https://www.smir.ch/BRATS/Start2015

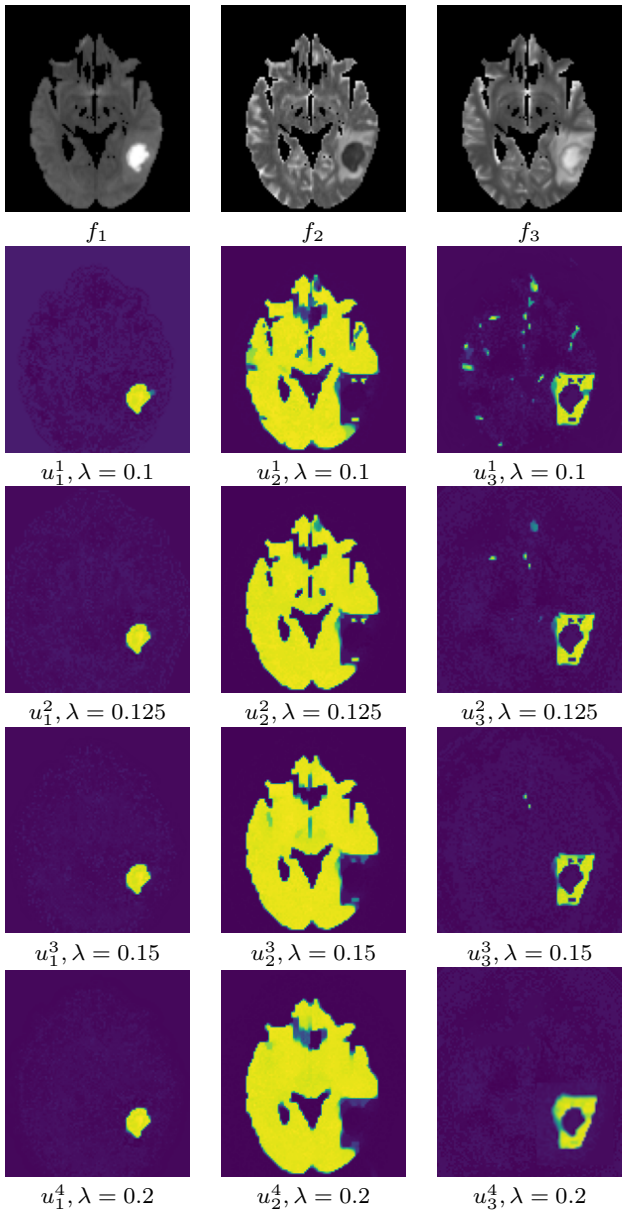

Fig. 14: In the first row the input images consisting of DWI, ADC and T2 images are visualized. The different rows show the results for different choices of the regularization parameter λ. From left to right we see the obtained (nearly binary) masks of abscess, healthy brain tissue and the edema.

the T1c (contrast-enhanced T1-weighted image), T2, and FLAIR (Fluid attenuated inversion recovery) image is given, each highlighting a different region of the tumor. Again, we exploit the information contained in the images of the different modalities by employing them as separate input channels. The proposed method is thus able to use this complementary information to delineate the different tissues and demonstrates solid results for this concrete example from medicine. The fact that the proposed energy functional can be applied directly to the given images, makes it particularly suitable for medical image segmentation.

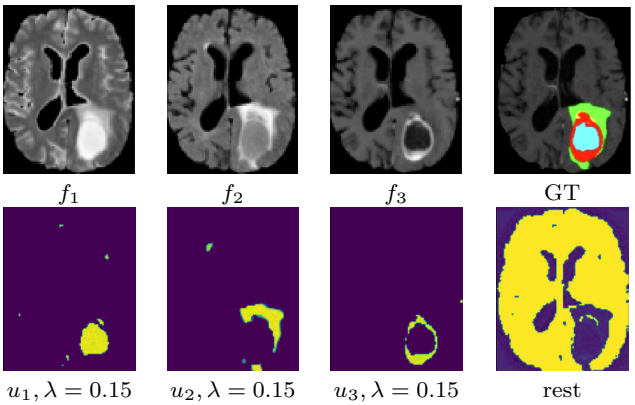

Fig. 15: The first row shows T1c, T2 and FLAIR images contained in the BRATS dataset, which are required for accurate tumor diagnosis and analysis as well as the ground truth annotations. The second row demonstrate the minimizers of the energy functional, presenting tumor, edema and necrosis. The last image represents the rest class.

7 Conclusion

In this paper, we have proposed a multichannel multiphase framework for image segmentation based on the active contour model introduced by Chan and Vese. The proposed framework is capable of performing segmentation of images consisting of several channels which can be given either in a natural form, such as RGB images, or can be extracted by some pre-filtering method. We demonstrated the effectiveness of our method on several images, such as artificial images containing texture or multi-modal medical images, and achieved convincing results, which were confirmed by good performance in comparison with other related approaches. The method can distinguish between up to $K + 1$ different regions, where K denotes the number of input channels, which makes it particularly suitable for applications in medical imaging. Further we have shown existence of minimizers and examined stability and convergence behavior with respect to the distorted input images. For future extension of the proposed framework, the combination with deep learning is planned, in particular, the feature maps extracted in this paper by means of pre-filtering shall be obtained by a neural network. The combination of the strengths of modern deep learning and classical energy based segmentation methods could further improve the existing results and enable more complex problems to be solved.

Acknowledgments

This study is supported by VASCage – Research Centre on Vascular Ageing and Stroke. As a COMET centre VASCage is funded within the COMET program - Competence Centers for Excellent Technologies by the Austrian Ministry for Climate Action, Environment, Energy, Mobility, Innovation and Technology, the Austrian Ministry for Digital and Economic Affairs and the federal states Tyrol, Salzburg and Vienna

References

1. Alberti, G., Bouchitté, G., Dal Maso, G.: The calibration method for the Mumford-Shah functional and free-discontinuity problems. Calculus of Variations and Partial Differential Equations **16**(3), 299–333 (2003)
2. Ambrosio, L.: Variational problems in sbv and image segmentation. Acta Applicandae Mathematica **17**(1), 1–40 (1989)
3. Ambrosio, L., Fusco, N., Pallara, D.: Functions of bounded variation and free discontinuity problems, vol. 254. Clarendon Press Oxford (2000)
4. Ambrosio, L., Tortorelli, V.M.: Approximation of functional depending on jumps by elliptic functional via t-convergence. Communications on Pure and Applied Mathematics **43**(8), 999–1036 (1990)
5. Brown, E.S., Chan, T.F., Bresson, X.: A convex relaxation method for a class of vector-valued minimization problems with applications to mumford-shah segmentation. Ucla cam report **10**(43) (2010)
6. Cai, X., Chan, R., Zeng, T.: A two-stage image segmentation method using a convex variant of the Mumford-Shah model and thresholding. SIAM Journal on Imaging Sciences **6**(1), 368–390 (2013)
7. Chambolle, A.: An algorithm for total variation minimization and applications. Journal of Mathematical imaging and vision **20**(1), 89–97 (2004)
8. Chambolle, A., Pock, T.: A first-order primal-dual algorithm for convex problems with applications to imaging. Journal of mathematical imaging and vision **40**(1), 120–145 (2011)
9. Chan, T.F., Esedoglu, S., Nikolova, M.: Algorithms for finding global minimizers of image segmentation and denoising models. SIAM journal on applied mathematics **66**(5), 1632–1648 (2006)
10. Chan, T.F., Sandberg, B.Y., Vese, L.A.: Active contours without edges for vector-valued images. Journal of Visual Communication and Image Representation **11**(2), 130–141 (2000)
11. Chan, T.F., Vese, L.A.: Active contours without edges. IEEE Transactions on image processing **10**(2), 266–277 (2001)
12. Evans, L.C., Gariepy, R.F.: Measure theory and fine properties of functions, vol. 5. CRC press Boca Raton (1992)
13. Gariepy, R.F.: Functions of bounded variation and free discontinuity problems (clarendon press, oxford, 2000). Bulletin of the London Mathematical Society **33**(4), 492–512 (2001)
14. Giusti, E.: Minimal surfaces and functions of bounded variation. Monogr. Math. **80** (1984)
15. Hammouda, K., Jernigan, E.: Texture segmentation using gabor filters. Cent. Intell. Mach **2**(1), 64–71 (2000)
16. Homayounfar, N., Xiong, Y., Liang, J., Ma, W.C., Urtasun, R.: Levelset r-cnn: A deep variational method for instance segmentation. In: European Conference on Computer Vision, pp. 555–571. Springer (2020)
17. Jain, A.K., Farrokhnia, F.: Unsupervised texture segmentation using gabor filters. Pattern recognition **24**(12), 1167–1186 (1991)
18. Kobler, E., Klatzer, T., Hammernik, K., Pock, T.: Variational networks: Connecting variational methods and deep learning. In: German conference on pattern recognition, pp. 281–293. Springer (2017)
19. Le, T.H.N., Quach, K.G., Luu, K., Duong, C.N., Savvides, M.: Reformulating level sets as deep recurrent neural network approach to semantic segmentation. IEEE Transactions on Image Processing **27**(5), 2393–2407 (2018)
20. Lee, S.I., Lee, H., Abbeel, P., Ng, A.Y.: Efficient l˜ 1 regularized logistic regression. In: Aaai, vol. 6, pp. 401–408 (2006)
21. Li, F., Ng, M.K., Zeng, T.Y., Shen, C.: A multiphase image segmentation method based on fuzzy region competition. SIAM Journal on Imaging Sciences **3**(3), 277–299 (2010)
22. Michelot, C.: A finite algorithm for finding the projection of a point onto the canonical simplex of $\mathbb{R}^n$. Journal of Optimization Theory and Applications **50**(1), 195–200 (1986)
23. Morel, J.M., Solimini, S.: Variational methods in image segmentation: with seven image processing experiments, vol. 14. Springer Science & Business Media (2012)
24. Moreno, J.C., Prasath, V.S., Proenca, H., Palaniappan, K.: Fast and globally convex multiphase active contours for brain mri segmentation. Computer Vision and Image Understanding **125**, 237–250 (2014)
25. Mory, B., Ardon, R.: Fuzzy region competition: A convex two-phase segmentation framework. In: International Conference on Scale Space and Variational Methods in Computer Vision, pp. 214–226. Springer (2007)
26. Mumford, D.B., Shah, J.: Optimal approximations by piecewise smooth functions and associated variational problems. Communications on pure and applied mathematics (1989)
27. Osher, S., Sethian, J.A.: Fronts propagating with curvature-dependent speed: algorithms based on hamilton-jacobi formulations. Journal of computational physics **79**(1), 12–49 (1988)
28. Ranftl, R., Pock, T.: A deep variational model for image segmentation. In: German Conference on Pattern Recognition, pp. 107–118. Springer (2014)
29. Rockafellar, R.T.: Convex analysis. 28. Princeton university press (1970)
30. Sandberg, B., Kang, S.H., Chan, T.F.: Unsupervised multiphase segmentation: A phase balancing model. IEEE transactions on image processing **19**(1), 119–130 (2009)
31. Valkonen, T.: A primal–dual hybrid gradient method for nonlinear operators with applications to mri. Inverse Problems **30**(5), 055012 (2014)
32. Vese, L.A., Chan, T.F.: A multiphase level set framework for image segmentation using the mumford and shah model. International journal of computer vision **50**(3), 271–293 (2002)
33. Wu, Y.: Chan Vese Active Contours without edges. `https://www.mathworks.com/matlabcentral/fileexchange/23445-chan-vese-active-contours-without-edges` (2021). [Online; accessed 22-June-2021]

34. Yuan, J., Bae, E., Tai, X.C., Boykov, Y.: A continuous max-flow approach to Potts model. In: European conference on computer vision, pp. 379–392. Springer (2010)
35. Zhu, S.C., Yuille, A.: Region competition: Unifying snakes, region growing, and bayes/mdl for multiband image segmentation. IEEE transactions on pattern analysis and machine intelligence **18**(9), 884–900 (1996)